Sentinel-1 vegetation optical depth retrievals over the international soil moisture network

Zhixuan Lu, Lei Fan, Xiangzhuo Liu, Xiaojing Bai, Nicolas Baghdadi, Frédéric Frappart, Jiangyuan Zeng, Gabrielle de Lannoy, Jian Peng, Zanpin Xing, et al.

International Journal of Digital Earth

ISSN: 1753-8947 (Print) 1753-8955 (Online) Journal homepage: www.tandfonline.com/journals/tjde20

Sentinel-1 vegetation optical depth retrievals over the international soil moisture network

Zhixuan Lu, Lei Fan, Xiangzhuo Liu, Xiaojing Bai, Nicolas Baghdadi, Frédéric Frappart, Jiangyuan Zeng, Gabrielle De Lannoy, Jian Peng, Zanpin Xing, Xiaojun Li, Zhuangzhuang Feng, Xin Li & Jean-Pierre Wigneron

To cite this article: Zhixuan Lu, Lei Fan, Xiangzhuo Liu, Xiaojing Bai, Nicolas Baghdadi, Frédéric Frappart, Jiangyuan Zeng, Gabrielle De Lannoy, Jian Peng, Zanpin Xing, Xiaojun Li, Zhuangzhuang Feng, Xin Li & Jean-Pierre Wigneron (2025) Sentinel-1 vegetation optical depth retrievals over the international soil moisture network, International Journal of Digital Earth, 18:2, 2555412, DOI: 10.1080/17538947.2025.2555412

To link to this article: https://doi.org/10.1080/17538947.2025.2555412

Published online: 21 Sep 2025.

INTERNATIONAL JOURNAL OF DIGITAL EARTH
2025, VOL. 18, NO. 2, 2555412
https://doi.org/10.1080/17538947.2025.2555412

Sentinel-1 vegetation optical depth retrievals over the international soil moisture network

Zhixuan Lu[a,b], Lei Fan[a,b], Xiangzhuo Liu[c], Xiaojing Bai[d], Nicolas Baghdadi[e], Frédéric Frappart[c], Jiangyuan Zeng[f], Gabrielle De Lannoy[g], Jian Peng[h], Zanpin Xing[c,i], Xiaojun Li[c], Zhuangzhuang Feng[a,b], Xin Li[j,k] and Jean-Pierre Wigneron[c]

[a]Chongqing Jinfo Mountain Karst Ecosystem National Observation and Research Station, School of Geographical Sciences, Southwest University, Chongqing, People's Republic of China; [b]Chongqing Engineering Research Center for Remote Sensing Big Data Application, School of Geographical Sciences, Southwest University, Chongqing, People's Republic of China; [c]ISPA, UMR 1391, INRAE Nouvelle-Aquitaine, Université de Bordeaux, Bordeaux, France; [d]School of Hydrology and Water Resources, Nanjing University of Information Science & Technology, Nanjing, People's Republic of China; [e]National Research Institute for Agriculture, Food and Environment (INRAE), UMR TETIS, University of Montpellier, Montpellier, France; [f]State Key Laboratory of Remote Sensing Science, Aerospace Information Research Institute, Chinese Academy of Sciences, Beijing, People's Republic of China; [g]Department of Earth and Environmental Sciences, KU Leuven, Heverlee, Belgium; [h]Remote Sensing Centre for Earth System Research, Leipzig University, Leipzig, Germany; [i]Center for the Pan-Third Pole Environment, Lanzhou University, Lanzhou, People's Republic of China; [j]CAS Center for Excellence in Tibetan Plateau Earth Sciences, Chinese Academy of Sciences, Beijing, People's Republic of China; [k]National Tibetan Plateau Data Center, State Key Laboratory of Tibetan Plateau Earth System and Resource Environment, Institute of Tibetan Plateau Research, Chinese Academy of Sciences, Beijing, People's Republic of China

ABSTRACT

Vegetation optical depth (VOD), a microwave-based vegetation index for vegetation water content and biomass, is primarily retrieved from low spatial resolution passive microwave data, and few studies have focused on VOD retrievals from active microwave data. The Sentinel-1 satellite is expected to provide long-term (more than 20 years) high-resolution (~10 m) C-band backscatter from 2014 onwards. In this study, a 1-km VOD retrieval was developed based on the Water Cloud Model, incorporating the Dubois model to represent soil backscatter. The main feature of the algorithm is the implementation of pixel-based soil parameters, coupled with annual vegetation parameters to enhance the retrieval accuracy. The algorithm was developed over the sites of the international soil moisture network during 2016–2022, where accurate soil moisture datasets could be used as input in the retrieval. Its temporal performance was evaluated by comparison with two optical vegetation indices: the normalized difference vegetation index and the enhanced vegetation index. Evaluation results demonstrated that the algorithm performed well for the VOD retrievals, and the highest correlation values between VOD and both vegetation indices could be particularly noted for grassland, with an average of 0.79. The evaluation highlighted the potential benefit of coupling WCM with a semi-empirical soil backscatter model for VOD retrieval.

ARTICLE HISTORY
Received 15 June 2025
Accepted 25 August 2025

KEYWORDS
Sentinel-1; vegetation optical depth; C-band; active microwave

1. Introduction

Vegetation optical depth (VOD) has been shown to be a reliable metric for measuring the extinction effects of the microwave (passive or active) radiations by the vegetation canopy. Evidence has demonstrated a positive correlation between VOD and both vegetation water content (VWC) and biomass (Frappart et al. 2020; Schmidt et al. 2023). Optical vegetation indices were not considered as an accurate proxy of total above-ground biomass (AGB), except in areas of low vegetation density (Todd, Hoffer, and Milchunas 1998). In contrast, being sensitive to both green and non-green vegetation components, microwave observations can provide important complementary information on the state and temporal changes of the vegetation features (Chang et al. 2023; Fan et al. 2024), in particular regarding the above-ground biomass dynamics

CONTACT Lei Fan leifan33@swu.edu.cn Chongqing Jinfo Mountain Karst Ecosystem National Observation and Research Station, School of Geographical Sciences, Southwest University, Chongqing 400715, People's Republic of China Chongqing Engineering Research Center for Remote Sensing Big Data Application, School of Geographical Sciences, Southwest University, Chongqing 400715, People's Republic of China

(Rodríguez-Fernández et al. 2018). Accordingly, the utilization of publicly available VOD products has been extensive in a number of applications including the study of carbon dynamics in the pantropic region (Qin et al. 2021) and on a global scale(Yang et al. 2023), vegetation phenology (Jones et al. 2011), and the trends of burned areas and fire risks (Fan et al. 2018).

Currently, the potential of VOD products derived from passive microwave observations to monitor vegetation dynamics and support agricultural management at local scales is limited by their coarse spatial resolution (~25 km – ~40 km) (Boitard et al. 2024). By contrast, active microwave remote sensing with Synthetic Aperture Radar (SAR) can provide complementary observation to estimate high-resolution VOD (< 1 km) (El Hajj et al. 2019). The Sentinel-1 C-band SAR has valuable potential for estimating high-resolution VOD (Zhou et al. 2022), benefiting from its fine spatial detail (5 m × 20 m in IW mode) and revisit time (6–12 days) (Torres et al. 2012). Furthermore, they demonstrate a reduced susceptibility to radio-frequency interference (RFI) in comparison with passive microwave systems, particularly those operating at lower frequencies, such as L-band (Li et al. 2021). Consequently, high-resolution Sentinel-1 VOD would be pivotal in the development of applications, utilizing high spatial resolutions of approximately 10 m (Wang et al. 2024).

For the SAR observations simulation, the Water Cloud Model (WCM) has emerged as the predominant simulation model (Attema and Ulaby 1978). The model is of a semi-empirical nature, and its function is to simplify the complex interactions between surface and vegetation layers. The WCM is advantageous for its computational efficiency and simulation accuracy at large scales. A previous study conducted VOD retrievals by WCM in agricultural fields (El Hajj et al. 2019). Following that initial pathway, the inclusion of different soil backscatter models in conjunction with WCM contributed to VOD retrievals at a large scale. This was attributable to the capacity of these models to discern the vegetation effects through vegetation transmissivity and soil effects, which were measured using soil moisture and roughness in the backscatter simulation over the study area (Bai and He 2015; Vreugdenhil et al. 2020). In recent studies, the Ulaby model was chosen to simulate the soil backscatter based on ASCAT (ASCAT-IB) at a global scale (Liu et al. 2021) and Sentinel-1 in the grassland of the Heihe River Basin (Zhou et al. 2022).

However, due to the inhomogeneity of soil characteristics at the scale of large landscapes (Wang et al. 2023), the parameterization of the soil backscatter model is a pivotal consideration in the practical implementation of the WCM. The Ulaby model establishes a linear relationship between soil backscatter and soil moisture. Two main parameters are used in the Ulaby model, which are the backscatter coefficient of bare soil in very dry conditions (C) and the sensitivity of backscatter observation to soil moisture variation (D). In the Sentinel-1 and ASCAT VOD retrieval, the number of pixels utilized for the calibration of the D value is obviously less than that employed for the calibration of the C value (Liu et al. 2021; Liu et al. 2023) and may result in certain issues, mainly in dry areas where soil moisture is almost constant and the D value is hard to calibrate (Liu et al. 2023). It is imperative that this critical component is given due consideration when parameterizing the Ulaby model. Consequently, the utilization of the Ulaby model in conjunction with the WCM for backscatter simulation can result in uncertainties in VOD estimates, with arid regions being particularly impacted.

As is evident in the extant literature, there are numerous models of soil backscatter. The objective of these models is to simulate radar backscatter and to facilitate the retrieval of soil surface characteristics from SAR imagery. The Dubois model is a semi-empirical model that is utilized for the purpose of simulating soil backscatter (Dubois, Van Zyl, and Engman 1995), and it has been used in soil moisture retrieval by combining it with WCM. Compared to the Ulaby model, the Dubois model is advantageous due to its applicability across diverse regions without dependence on region-specific soil conditions. However, the data and site dependency of the Dubois model make it limited in applications (Dubois, Van Zyl, and Engman 1995; Zribi et al. 2005). Considering the advantages of the Dubois models over the Ulaby model, this study explores the potential of the Dubois model for VOD retrieval. In this regard, a semi-empirical algorithm is constructed to establish a relationship between co-polarized backscatter and VOD, as well as soil dielectric constant (Bai and He 2015; Liu and Shi 2016).

In addition, most of the current works have concentrated on the retrieval of VOD at either the regional or global scale. As the high-resolution soil moisture input required to retrieve the high-resolution VOD is not available at a large scale, in most cases, the VOD retrieval models have been calibrated using coarse-resolution soil moisture data (Zhou et al. 2022). This results in the utilization of identical soil moisture values

across disparate sites within each pixel, whilst disregarding the considerable within-pixel heterogeneities of variations in climate and soil properties.

In this study, we investigated the potential of using WCM coupled with the Dubois model (hereafter 'WCM + Dubois') for high-resolution VOD retrievals from Sentinel-1 SAR data at the site scale. We focused our study on sites of the International Soil Moisture Network (ISMN) where accurate soil moisture data are available as input to our retrieval model for a large variety of conditions in terms of soil moisture and vegetation types (Dorigo et al. 2013). The main objective here is to specifically assess the variation in the performance of VOD retrievals under diverse vegetation conditions.

2. Data

2.1. In-situ *soil moisture networks*

The ISMN was initiated in order to support the calibration/validation activities of remotely sensed products. It is a collaborative initiative aimed at establishing and maintaining a global in-situ soil moisture database (Dorigo et al. 2021). In the retrieval, we used in-situ surface moisture datasets from 2016 to 2022 at a depth of 0–5 cm from 53 stations in the ISMN network. To guarantee the accuracy of the input data for the retrieval process, only in-situ soil moisture data marked as 'Good' were considered from the ISMN (Dorigo et al. 2011; Figure 1). To minimize temporal mismatch between *in-situ* data and satellite overpasses, only average soil moisture values within a 5-hour window centered on each satellite observation were used.

2.2. Sentinel-1 data

The VOD retrieved from VV-pol data has been shown to better capture vegetation temporal dynamics than VH-pol data, as evidenced by previous studies on VOD retrieval using C-band Sentinel-1 data (El Hajj et al. 2019). Thus, in this study, the Sentinel-1A GRD IW data at descending orbit for VV polarized backscatter (σ^0_{VV}) and incidence angle from 2016 to 2022 were obtained. The ESA Sentinel-1 toolbox was used to preprocess Sentinel-1 images, minimizing error propagation in subsequent processes by applying an orbit file, thermal noise removal, border noise removal, radiometric calibration, speckle filter and terrain correction (Filipponi 2019). This workflow transforms SAR image digital numbers into linear backscatter coefficients (El Hajj et al. 2019). Given that the retrieval process necessitates the analysis of a voluminous dataset, and considering the inherent uncertainty of Sentinel-1 data (Benninga, van der Velde, and Su 2019), a constraint was included to filter annual Sentinel-1 datasets, prioritizing datasets with a correlation coefficient between backscatter and NDVI over 0.5 to balance the trade-off between retrieval time and accuracy. The datasets were resampled to 1 km spatial resolution through nearest neighbor interpolation.

Sentinel-1 has the capacity to acquire diverse strips with a scheduling time horizon, given that the satellite possesses the capability to traverse the target on multiple occasions. The strip is defined in terms of

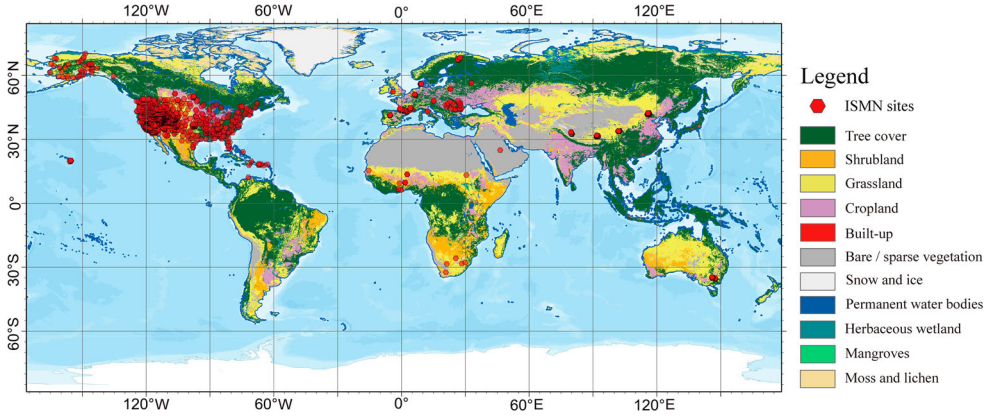

Figure 1. Spatial distribution of the ISMN sites. The overlaid European Space Agency (ESA) WordCover land cover map is based on the Land Cover Classification System [21], which was combined into 11 land types.

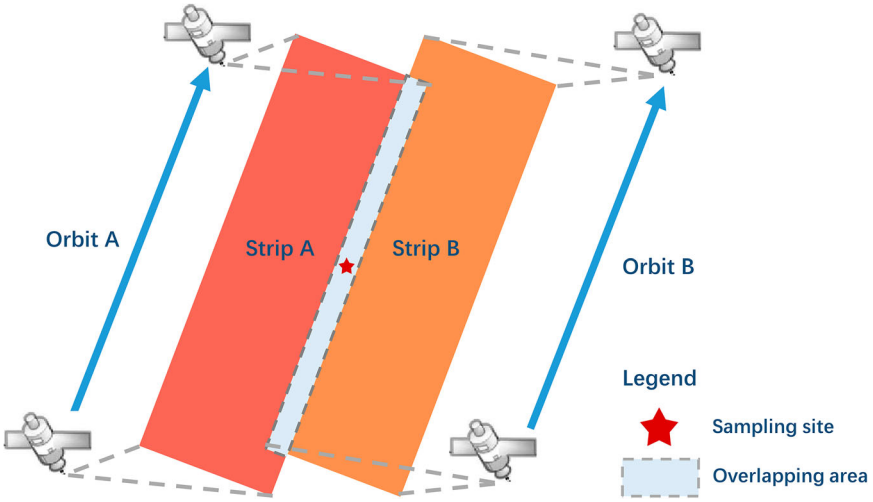

Figure 2. Strips with different orbits for the sampling sites in overlapping areas.

geometry and is directly associated with image acquisition. It is evident that the Sentinel-1 observation across the sampling sites in the overlapping area between two strips exceeds one orbit, as presented in Figure 2. Here, the Sentinel-1 orbit code, which represents the strip's index of observation data, was also used in this study.

2.3. Vegetation index data

As there is no large-scale in-situ dataset of VOD, a proxy is needed for the validation of VOD (Li et al. 2021). Several studies have shown that the temporal dynamics of VOD are a good indicator of the vegetation phenology as monitored from optical vegetation indices(Jones et al. 2011; Lawrence et al. 2014). Thus, the optical indices can be used as the benchmark to assess the performance of retrieved VOD (Frappart et al. 2020; Wigneron et al. 2024). Different vegetation indices, including both Normalized Difference Vegetative Index (NDVI) and Enhanced Vegetation Index (EVI), were used to assess the performance of VOD in temporal terms. Specifically, the 8-day NDVI and EVI data at 1 km spatial resolution calculated from MOD13A2 (Didan 2015a) and MYD13A2 products (Didan 2015b) were used in this study. These datasets were filtered to exclude pixels with errors. High-quality pixels can be identified by referencing the quality control (QC) layer.

Considering the inconsistency in the overpass time of MODIS and Sentinel-1, the temporal alignment of the VIs data was conducted in accordance with the temporal proximity of the closest Sentinel-1 observation. The temporal alignment of each VI product and Sentinel-1 data was constrained to a maximum time interval of 4 days, with the assumption that VIs were stable during the 4 days (El Hajj et al. 2019).

2.4. Soil properties and land cover data

The SoilGrids250 m dataset is a global dataset of standardized soil properties, measured at different standard depths, with a spatial resolution of 250 meters (Poggio et al. 2021). The bulk density, clay particles and sand particles from the top layer (0–5 cm) of the SoilGrids250 m dataset were used in the soil backscatter simulation of the Dubois model.

As demonstrated by numerous preceding studies, the feature of VOD is contingent upon the specific characteristics of the land cover (Li et al. 2021; Vreugdenhil et al. 2016). The land cover data from the ESA WorldCover dataset was used in the evaluation of VOD retrieval (Zanaga et al. 2022). The ESA WorldCover dataset offers global land cover information at a spatial resolution of 10 meters. These maps are obtained from the combination of microwave Sentinel-1 radar data and optical Sentinel-2 imagery. The classification maps, which are discrete in nature, provide 11 classes that have been defined using the

Land Cover Classification System. The Land Cover Classification System was defined by the United Nations Food and Agriculture Organization (Di Gregorio 2005).

To address the resolution mismatch, all image datasets were resampled to a spatial resolution of 1 km using a nearest neighbor interpolation based on pixels corresponding to ISMN sites.

3. Methods

3.1. Water cloud model

In the implement of WCM (Attema and Ulaby 1978), the total backscattering coefficient (σ^o_{obs} in linear units) received by the Sentinel-1 sensor can be decomposed into two components (Equation (1)): the vegetation backscatter (σ^o_{vege}) (Equation (2)) and soil backscatter signal reduced by the vegetation canopy (σ^o_{soil}). The attenuation of vegetation is denoted as the vegetation transmissivity (τ^2), which can be treated as a function of the incidence angle (θ) of Sentinel-1 data and VOD (Equation (3)) as given below:

$$\sigma^o_{obs\ (linear)} = \sigma^o_{vege} + \tau^2\sigma^0_{soil} \tag{1}$$

$$\sigma^0_{vege} = AV_1\cos\theta(1-\tau^2) \tag{2}$$

$$\tau^2 = \exp\left[\frac{-2VOD}{\cos\theta}\right] \tag{3}$$

where A is the backscatter of vegetation canopy at a very dense vegetated (VDV) period, V_1 is the index that can be set to 1 (Attema and Ulaby 1978).

The VDV period was defined as the date on which the NDVI value exceeded the 75th percentile of the NDVI time series for each pixel. It can be assumed that, given the observed characteristics of the vegetation, the transmissivity is likely to be negligible over the VDV period (Liu et al. 2021). Thus, we assumed that the σ^o_{soil} is completely attenuated, thus allowing the σ^o_{vege} can be set equal to the σ^o_{obs}, Equation (2) could be simplified as:

$$\sigma^o_{obs} = \sigma^o_{vege} = A\cos\theta \tag{4}$$

where the value of A for the VDV period (referred to as A_0) can be expressed as:

$$A_0 = \frac{\sigma^o_{obs}}{\cos\theta} \tag{5}$$

Daily A for a given pixel ($A(i, j, t)$) was set homogeneously equal to the 95th percentile of A_0 over VDV period ($A_0^{95\%}(i, j)$) for each pixel in Equation (6):

$$A(i, j, t) = A_0^{95\%}(i, j) \tag{6}$$

Equations (2)-(3) were inserted into Equation (1), and σ^o_{obs} can be expressed as:

$$\sigma^o_{obs} = AV_1\cos\theta\left(1-\exp\left[-\frac{2VOD}{\cos\theta}\right]\right) + \exp\left[-\frac{2VOD}{\cos\theta}\right]\sigma^0_{soil} \tag{7}$$

And VOD can be computed as using a constant A (Figure 3):

$$VOD = -\frac{1}{2}\cos\theta\ln\left(\frac{\sigma^o_{obs} - A\cos\theta}{\sigma^0_{soil} - A\cos\theta}\right) \tag{8}$$

3.2. Soil scattering model

The Dubois model characterizes the HH-pol and VV-pol backscatter from soil surfaces as a function of surface roughness (RMS height of soil surface, s), dielectric constant (ε), incidence angle (θ) and sensor frequency of Sentinel-1 (Dubois, Van Zyl, and Engman 1995), and VV-pol backscatter (σ^0_{VV}) is expressed as:

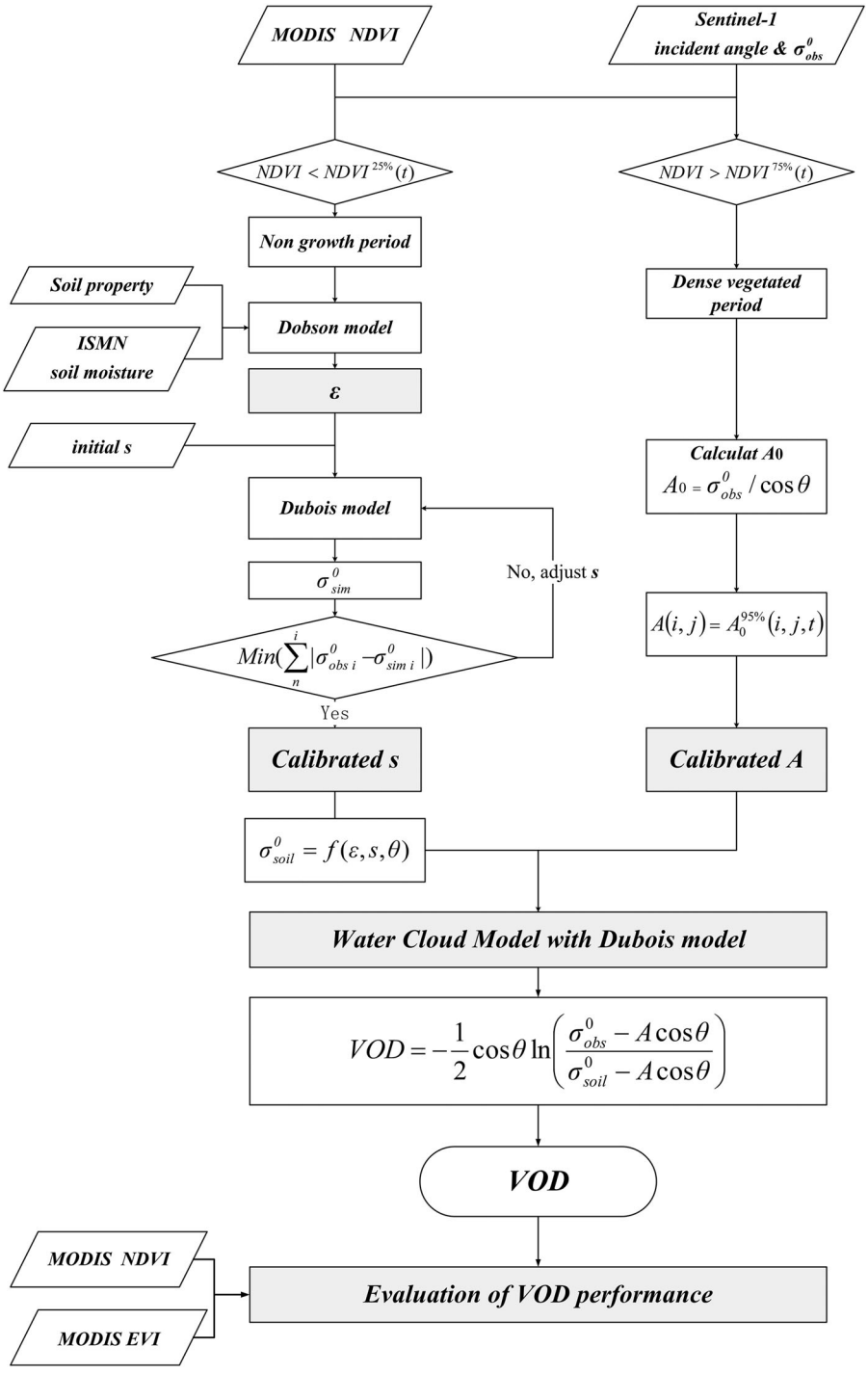

Figure 3. Flowchart of VOD retrieval based on the WCM and Dubois model.

$$\sigma^0_{VV} = 10^{-2.35}\frac{(\cos\theta)^3}{(\sin\theta)^3}10^{0.046\varepsilon tan\theta}(ks \times \sin\theta)^{1.1}\lambda^{0.7} \quad (9)$$

where k is the wave number, and λ is the wavelength (Dubois, Van Zyl, and Engman 1995).

The Dobson model was employed to derive ε (ε_d) (Dobson et al. 1985), the detailed expression with respect to the real part of ε_d (ε'_d) and imaginary part of ε_d (ε''_d) for the Dobson model could be defined as follows:

$$\varepsilon_d' = \left[1 + \frac{\rho_b}{\rho_s}(\varepsilon_s^{\alpha} - 1) + m_v^{\beta'}\varepsilon_{fw}'^{\,a} - m_v\right]^{1/\alpha} \tag{10}$$

$$\varepsilon_d'' = [m_v^{\beta''}\varepsilon_{fw}''^{\,a}]^{1/\alpha} \tag{11}$$

where $\alpha = 0.65$ is a shape factor, ρ_s and ρ_b are the soil particle density and soil bulk density from SoilGrids250 m, respectively, ε_s denotes the dielectric constant of soil solid phases, while m_v represents the soil volumetric water content obtained from ISMN, β' and β'' are the adjustable parameters related to soil properties, ε_{fw}' and ε_{fw}'' refer to the real and imaginary parts of the dielectric constant of water in the soil, derived by the Debye function (Lane and Saxton 1952).

The ε was finally inserted into Equation (9), the VV-pol bare soil backscatter in linear units for the Dubois model ($\sigma^0_{VV-soil}$) can be formulated as:

$$\sigma^0_{VV-soil} = 10^{-2.35}\frac{(\cos\theta)^3}{(\sin\theta)^3}10^{0.046tan\theta\varepsilon_d}(ks \times \sin\theta)^{1.1}\lambda^{0.7} \tag{12}$$

In the retrieval, the parameter s has to be calibrated on each ISMN site. To calibrate the s parameter, we first computed the values of the ε, with the assumption that vegetation effects can be neglected during the non-growing season, and we calibrate s annually. The steps are summarized in Figure 3.

Step 1: annually select the non-growing season based on the NDVI data from 2016 to 2022. For each pixel, the annual non-growing season was defined as the period when vegetation was relatively sparse. The annual sparse vegetation period was identified as the period when the NDVI values are lower than the 25th percentile of the time series. To be noted, we did not perform s calibration and VOD retrievals in pixels where NDVI values are higher than 0.2 throughout certain years to make sure the vegetation effect can be neglected.

Step 2: annually estimating s for pixels corresponding to ISMN. For the pixels corresponding to ISMN, the ε could be obtained by soil moisture from ISMN, soil properties from SoilGrids250 m and σ^0_{obs} from Sentinel-1 (Equation (10)). The only unknown input in the soil backscatter simulation is s. By assuming that the s was constant throughout the year (Zhu et al. 2019), the annual s for each pixel was derived by minimizing the average of the absolute differences between the observed and simulated σ^0_{soil} during the non-growing season (van der Velde et al. 2012).

With the completion of the calibration of s, the expression of $\sigma^0_{VV-soil}$ (Equation (12)) was finally inserted into Equation (8), the VOD retrieval based on WCM coupled with the Dubois model ($\mathrm{VOD_{Dubois}}$) can be expressed as Equation (13):

$$VOD_{Dubois} = -\frac{1}{2}\cos\theta ln\left(\frac{\sigma^o_{obs} - A\cos\theta}{10^{-2.35}\frac{(\cos\theta)^3}{(\sin\theta)^3}10^{0.046tan\theta\varepsilon}(ks \times \sin\theta)^{1.1}\lambda^{0.7} - A\cos\theta}\right) \tag{13}$$

3.3. Evaluation metrics

The temporal Pearson correlation coefficient (R) with ancillary VIs (Equation (14)) and the standard deviation of R were used as metrics to assess the retrieval performance. The study's statistical significance was determined by the p-value, with a threshold of $p < 0.05$ considered to indicate a statistically significant correlation.

$$R = \frac{\sum_{i=1}^{n}(VOD_i - \overline{VOD})(Y_i - \bar{Y})}{\sqrt{\sum_{i=1}^{n}(VOD_i - \overline{VOD})^2}\sqrt{\sum_{i=1}^{n}(Y_i - \bar{Y})^2}} \tag{14}$$

where Y is VIs, i is a sequence of pixels, n is the number of valid pixels where s and daily A parameters can be retrieved, as well as the VOD, Y_i and VOD_i are the evaluation data or vegetation optical depth values of the

sequence at the i_{th} location, respectively. $\bar{Y}$ and $\overline{VOD}$ are the mean values of evaluation data and vegetation optical depth, respectively.

4. Result

4.1. Calibration results of parameters

To calibrate the vegetation parameter A of the WCM model over ISMN, the A_0 values were first computed using Equation (5) over the very dense vegetated (VDV) period for each site, and then the 95th percentile was calculated. As illustrated in Figure 4, the high values parameter A is predominantly concentrated in the western region of North America, a geographical area characterized by a predominant forest composition (Figure 1). In this study, the parameter calibration was made for each year. Annual A of each site exhibited a greater number of maximum values in 2018, while a greater number of minimum values were obtained in 2019, coinciding with the nadir of the Sentinel-1 backscatter.

To facilitate a comprehension of the variances in the A parameter across the vegetation types. Table 1 summarizes the mean, maximum and minimum values of parameter A over ISMN sites for each vegetation type. As presented in the table, the average A values over the forest are obviously higher than those over other vegetation types. Small variability in A values can be noted for shrubland, grassland and cropland.

4.2. Spatial pattern of VOD retrieval

The spatial distribution around worldwide ISMN stations presented in this study illustrated the summertime average values of retrievals and observations for pixels corresponding to ISMN sites (Figure 5). On a global scale, VOD retrievals exhibited analogous spatial patterns to Sentinel-1 backscatter (Figure 5(a and b)), with low values in Asia and high values in the western part of North America (e.g. Wyoming). Conversely, an opposing pattern were observed in the spatial distribution of the calibrated s and soil moisture (Figure 5(c and d)), especially in the inland basins of Utah. In terms of partial correlation, VOD exhibited a significant positive correlation with backscatter coefficient (R values of 0.65) and a negative correlation with calibrated s and soil moisture (R values of – 0.28 for soil moisture and – 0.36 for s, respectively).

Nevertheless, it should be acknowledged that there are exceptions to this pattern, particularly in the Rocky Mountains, where there is a distribution of low VOD values. The spatial pattern of VOD is analogous to that of calibrated soil moisture and soil moisture. It could be concluded that the relationship between VOD and two soil backscatter simulation inputs was not well reflected in western Colorado.

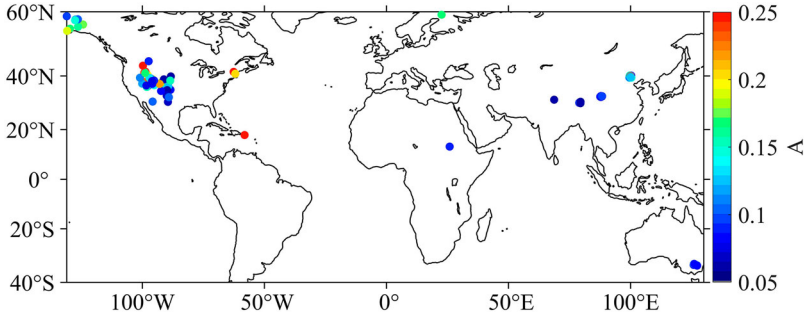

Figure 4. Map showing time-averaged values of calibrated A over ISMN sites.

Table 1. Average of calibrated A with respect to mean, maximum and minimum values for different land cover

Land cover	A_{Mean}	A_{MAX}	A_{MIN}
Forest	0.17	0.20	0.15
Shrubland	0.11	0.13	0.08
Grassland	0.09	0.12	0.07
Cropland	0.10	0.14	0.07

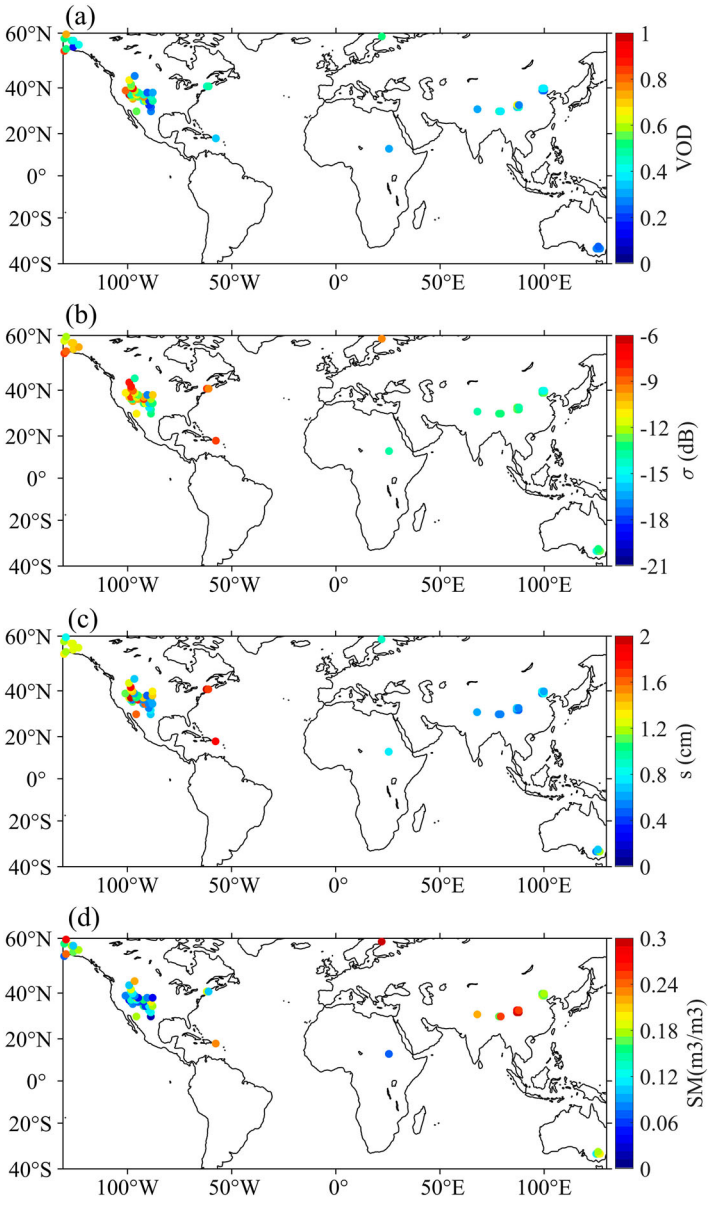

Figure 5. Maps showing time-averaged summer values of retrievals and observations at the ISMN sites for VOD (a), backscatter coefficient (b), calibrated *s* (c) and soil moisture (d).

Table 2. Temporal correlation (R) and standard deviation (STD) between the retrieved VOD with respect to NDVI and EVI for different land cover. Note that all correlation values are significant correlation with the 0.05 confidence level ($p < 0.05$).

	R_{VIs}		$STD(R_{VIs})$	
Land cover	R_{NDVI}	R_{EVI}	$STD(R_{NDVI})$	$STD(R_{EVI})$
Forest	0.70	0.73	0.14	0.06
Grassland	0.79	0.79	0.12	0.13
Cropland	0.76	0.78	0.12	0.15
All	0.77	0.78	0.14	0.13

4.3. Evaluation of VOD retrievals

Although the limited number of sites used for VOD retrieval in this study may not be enough to reveal the dependence of VOD retrieval on land cover, a thorough investigation was conducted into the specific performance of different land cover types in the retrieval process. The investigation encompassed the statistics of the average correlation coefficients with VIs (Table 2) and analysis of seasonal dynamics (Figure 6).

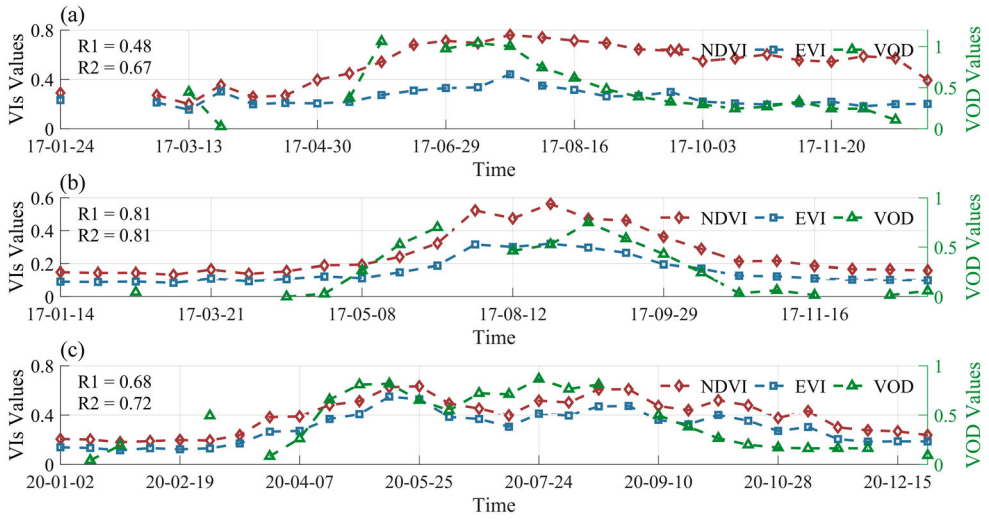

Figure 6. Temporal series of VOD and VIs for a grid cell over selected pixels. a-c, Temporal series of VOD and VIs over selected forest site (a), grassland site (b) and cropland site (c). Each plot contains VOD, NDVI and EVI series. R1 denotes the correlation between VOD and NDVI, while R2 denotes the correlation between VOD and EVI.

As illustrated in Table 2, the average values and standard deviation of R between VOD and VIs were derived from three major categories of land cover (e.g. forest, grassland and cropland). Our results indicated that the performance of the R values between VOD and VIs exhibited varied performance across different land cover types. Specifically, regarding the statistical average R values between VOD and VIs, grassland sites performed best compared to cropland and tree cover, with the highest R values with both VIs (R_{NDVI} = 0.79 ± 0.12, R_{EVI} = 0.79 ± 0.13), suggesting a strong relationship between retrieved results and vegetation features, followed by cropland sites with R_{NDVI} = 0.76 ± 0.12 and R_{EVI} = 0.78 ± 0.15. Then, forest sites followed with R_{NDVI} values of 0.70 ± 0.14 and R_{EVI} values of 0.73 ± 0.06, respectively.

Seasonal dynamics of retrieved VOD were further illustrated by plotting time series of VOD with respect to both NDVI and EVI at representative sites of the three main land covers (Figure 6).

Regarding the different sites, it is worth noting that the performance of the VOD in monitoring vegetation water content (VWC) varies from one site to the other (Figure 6). Considering the seasonal dynamics, the retrieved VOD from forest (Figure 6(a)) varied at a daily time-scale and did not effectively capture the dynamics of vegetation features during the periods of vegetation growth (June – August). This may partly be attributed to the fact that the vegetation backscatter exists in the forest throughout the year, even in the non-growing period. For the grassland site (Figure 6(b)) and cropland site (Figure 6(c)), the seasonal dynamics of the VODs were highly synchronous with the VIs, thus effectively capturing the dynamics of the vegetation feature. This suggests that distinct coupling strategies exist between vegetation and trees across diverse land types.

5. Discussion

5.1. Key factors affecting VOD retrieval performance

Our evaluation results present the difference in VOD performance across different land covers. The difference in VOD performance in monitoring VWC over different land cover could be partly explained by the environment and observation conditions. Here, we focused on the impacts of the Sentinel-1 observation orbit, backscatter correlation with VIs, soil moisture and NDVI on the retrieval.

For the purposes of the analysis below, we analyzed results from the areas where the two orbits overlapped (Figure 2). One is referred to as strip A (the overlap of the top right corner of the previous scene) and the other as strip B (the overlap of the bottom left corner of the current scene). Therefore, in terms of satellite observation, the VOD datasets for the overlapping areas in each scene were uniformly distinguished as Orbit A or Orbit B, according to the observation orbit code for each strip.

5.1.1. Sentinel-1 observation orbit

Firstly, to confirm the impact of the observation orbits on the VOD retrieval accuracy, we compared scatter slopes of VOD and NDVI as well as the performance of VOD retrieval (the latter was represented by the R values between the VOD and the NDVI) across strips. This section focuses exclusively on the VOD datasets that were retrieved from areas where two strips overlap (Figure 2) and demonstrate a significant correlation (p-value < 0.05) with the VIs.

To quantitatively describe the effect of observation orbits on the VOD performance, the annual statistics (correlation and slope) were computed between both retrieved VODs of two observation orbits and NDVI, respectively, for each VOD dataset retrieved from Sentinel-1 data at descending orbits (Figure 7). It should be noted that the VODs have different sampling dates across observation orbits.

Despite the inconsistency in sampling date, it is evident that there was a large difference between VODs across observation orbits. The average relative difference in correlations between two VODs and NDVI reached 21.2% (Figure 7(a)). The relative difference in slopes between two VODs and NDVI is 43.9%, which is larger than that in correlation (Figure 7(b)).

As illustrated in Figure 8, the difference in correlation between VOD and NDVI is shown to be related to the difference in incidence angle. This is consistent with the fact that the observed backscatter is dominated by the factors, including incidence angle and topography (Atwood et al. 2014; Zhang et al. 2020). Therefore, uncertainty in the observations influences the retrieval of VOD. This also demonstrates that the difference in observation orbits has a non-negligible effect, which could potentially lead to a 60% difference in VOD performance in the worst case (Figure 7).

5.1.2. Backscatter correlation with NDVI

Secondly, the implementation of the retrieval method is complicated by the different relationships between the VOD and SAR signals, which vary depending on the properties of the vegetation (Rötzer et al. 2017; Zhong et al. 2024). Thus, we investigate the backscatter correlation with NDVI and the performance of retrieved VOD to explore the influence of satellite signal on the VOD retrieval. In this study, the correlation between retrieved VOD and NDVI, as well as EVI, was investigated. The VOD performance was analyzed in relation to the correlation between backscatter and NDVI, and the results were plotted to provide a comprehensive overview (Figure 9).

As demonstrated in a previous study (Vreugdenhil et al. 2020), there is a clear and significant correlation between the performance of VOD and the characteristics of signals, which could be partly explained by the

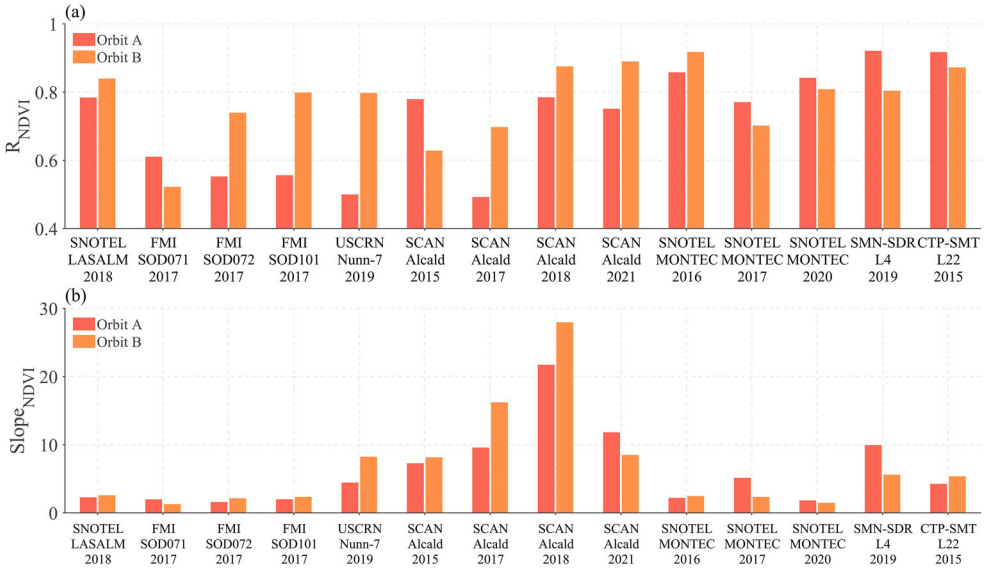

Figure 7. Metrics of all datasets for VODs retrieved from different observation orbits of the same site compared to VIs. a, Correlation R values between NDVI and VODs for two observation orbits of each dataset. b, Slope between NDVI and VODs for two observation orbits of each dataset. The dataset's information represented by networks, sites and years was shown on the axis. Orbit A and Orbit B represented the two observation orbits of the same site.

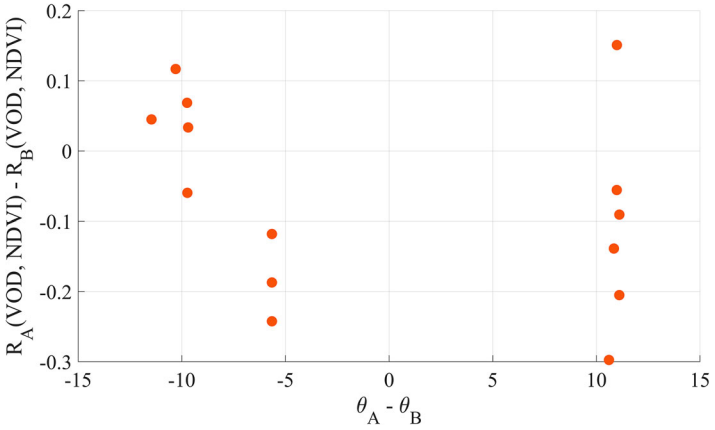

Figure 8. Scatterplots of the relationship between the difference in correlation coefficients and the difference in incidence angles of two orbits (Orbit A and Orbit B) at sampling sites within overlapping areas.

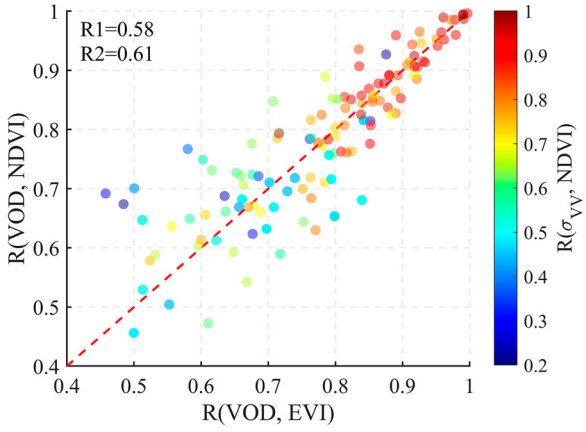

Figure 9. Scatterplots of correlation between VOD and VIs. The colors of the symbols represent backscatter correlation with NDVI. R1 denotes the R values between the correlation of VOD with NDVI and the correlation of backscatter with NDVI, while R2 denotes the R values between the correlation of VOD with EVI and the correlation of backscatter with NDVI. The correlation values are statistically significant at the 95 percent confidence level ($p < 0.05$).

fact that a significant correlation was identified between the VOD and σ^0_{VV} (Schmidt et al. 2024; Zhong et al. 2024). With the increase of the correlation between backscatter and NDVI, the retrieval performance increases more rapidly (Figure 9). A relationship was obtained between the correlation of VOD with VIs and the correlation of backscatter with NDVI, evidenced by the significant correlation coefficient of 0.58 for NDVI correlation performance and 0.61 for EVI correlation performance. These coefficients indicate that there is a lack of representativeness of VIs for the area where backscatter exhibited low correlation with vegetation features. This suggests that when all vegetation categories are considered collectively, a robust correlation exists between the vegetation representativeness of the observed signal and the retrieval performance (Rötzer et al. 2017). The Sentinel-1 signals (even after the preprocess) are heterogeneous, and this, in combination with the fact that stable signals are required to distinguish the contribution of vegetation and soil in the VOD retrieval (Xing et al. 2021), leads to a requirement for the properties of the Sentinel-1 backscatter signals in the retrieval algorithm.

5.1.3. Soil moisture

Thirdly, we evaluated the percentage of simulated soil backscatter falls below or above the total backscatter to explore and illustrate the effect of the accuracy of soil backscatter simulation on the VOD retrieval.

Soil moisture affects the VOD retrieval in the way that, with the increase of *in-situ* soil moisture, the simulated soil backscatter of the Dubois model increases exponentially. For the pixels with high *in-situ* soil moisture, the simulated soil backscatter could be higher than the observed backscatter.

The WCM that is used to simulate the backscatter coefficient in the VOD retrieval decomposes the total backscatter into the vegetation backscatter and the soil backscatter. In the retrieval, the overestimated soil backscatter data that exceeded the total backscatter were neglected, as it is hard to retrieve positive VOD values by the WCM based on these data (Equation (13)). However, the difference between total backscatter and simulated soil backscatter decreases exponentially with average soil moisture (Figure 10(a)).

To facilitate analysis of the impact of soil moisture on the retrieval process, the percentage of simulated soil backscatter that falls below or above the total backscatter was systematically categorized based on distinct soil moisture levels (Figure 10(b)). A consistent increasing trend of the percentage of the soil backscatter data that exceeded the total backscatter was generally observed. The percentage of overestimated soil backscatter is around 28% at high soil moisture levels in this study (soil moisture > 0.35). This may be attributed to the fact that the C-band SAR signal increases with humidity up to a threshold of 30-35%, beyond this threshold, the signal stabilizes and then begins to decrease (Bazzi et al. 2024). This effect under extremely wet conditions has also been confirmed by previous studies comparing C-band modeled backscatter with *in-situ* soil moisture (Aubert et al. 2012). These results clearly present that the overestimation of soil backscatter in VOD retrievals has a non-negligible effect, which may potentially lead to a deficiency of retrieval results (Figure 9(b)). Thus, better consideration of soil backscatter simulation, like a physics-based backscatter model over high soil moisture areas, should be taken into account in the future enhancements to our algorithm (Chen et al. 2003). In this study, the number of invalid results retrieved by high soil moisture data is comparatively low in relation to the number of

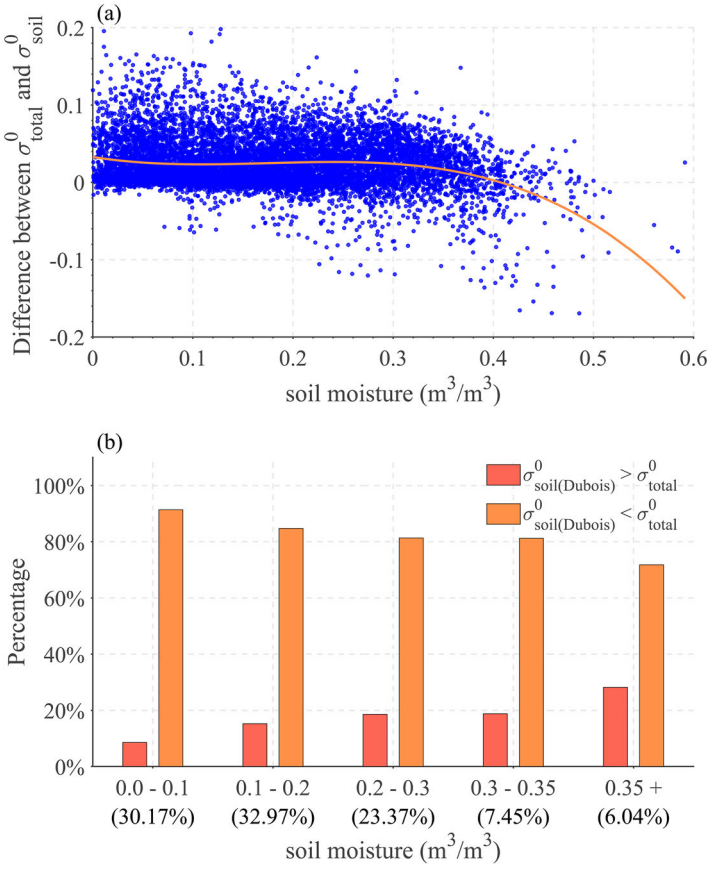

Figure 10. Analysis of soil moisture influence on VOD retrieval. a, Scatterplots of the difference between total and simulated soil backscatter with soil moisture. The solid red line is the predictive fit obtained by backscatter difference and soil moisture. b, Bars of the percentage of both simulated soil backscatter below or above total backscatter stratified by soil moisture levels. The percentages of points for different soil moisture levels are shown on the axis.

valid results. It was determined that there were sufficient retrieval results to quantitatively explore the performance of the algorithm. Therefore, the Dubois model was employed in this study to simulate the soil backscatter. It should be noted that there may be uncertainty in the VOD retrievals. This is due to the spatial representativeness error of *in-situ* soil moisture data, which is caused by the heterogeneity of the underlying surface (Peng et al. 2024).

5.1.4. NDVI

Finally, we analyzed the correlation between VOD and VIs at each NDVI level to quantitatively describe the effect of NDVI on the accuracy of the retrieval. The impact of average NDVI levels on the performance of the correlation between VOD and VIs is shown (Figure 11). It was evident that a decline in the correlation between VOD and both vegetation indices was observed as NDVI values increased (Li et al. 2021). It is worth noting that the relative variation in correlation between VOD and NDVI reached 22%. Specifically, the average correlation between VOD and NDVI decreases from R ∼ 0.79 to ∼ 0.62 as NDVI increases. Moreover, a broad quantitative range is observed for the correlation between VOD and NDVI, particularly at low NDVI levels (ranging from 0.2–0.3) or high NDVI values (interval from 0.5–0.6). Overall, the algorithm performed well in general, with average correlation coefficients between retrieved VOD and both VIs exceeding 0.77. The decrease in the evaluation results of the retrieved VOD with the increase of average NDVI values could be partly explained by the saturation of optical data in areas with high vegetation coverage (Tian et al. 2016).

5.2. Implications and outlook

The main purpose of this study is to evaluate the accuracy difference in VOD retrieval across different vegetation types. This is achieved by undertaking a comparative analysis of the VOD retrieved by a newly developed semi-empirical algorithm with reference to MODIS optical vegetation indices. In keeping with the evaluation of aforementioned studies, relatively higher correlation values and smaller errors were observed for the ISMN site over semi-arid regions, including grassland and cropland (Zhong et al. 2024). This suggests that the VOD retrieval based on the semi-empirical model in semi-arid regions, which are frequently labeled as low vegetation coverage, provides important information that catches well the temporal changes of the observed vegetation dynamics (Zhou et al. 2022).

While the model presented in this study yields favorable outcomes, opportunities for further improvement include:

(1) Optimization of data input. In the most recent advancements in VOD retrieval research, the models concern two unknown parameters in the retrieval: VOD and soil moisture (Li et al. 2022). For this study, the soil moisture was adopted as input, aligning with the spatial resolution of the retrieved

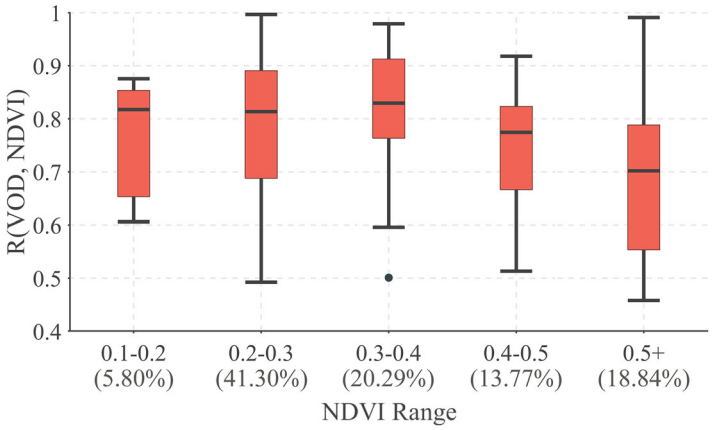

Figure 11. Boxplots of the correlation between VOD and NDVI stratified by NDVI levels. The percentages of datasets for different NDVI levels are shown in the axis.

VOD. Given that the site-scale soil moisture datasets were not available across continents (Xing et al. 2021), typically available at the global scale. In future work, we will extend to explore the VOD and soil moisture retrieval algorithm, aiming for a more comprehensive retrieval process and less datasets input.

(2) Fusion of VOD data from multiple satellites. Both ASCAT and Sentinel-1 can deliver C-band backscatter observation. The temporal resolution of Sentinel-1 VOD was limited by the revisit time of the satellite (El Hajj et al. 2019). An introduced long-term VOD product, ASCAT-IB VOD (Liu et al. 2021), can accommodate prolonged temporal information, which can make up for the low temporal resolution of Sentinel-1 VOD in the retrieval (Liu et al. 2023). In the future, we will consider data fusion and gap-filling of ASCAT and Sentinel-1 VOD in the retrieval.

As mentioned above, the regional scale 1-km VOD could be retrieved by the improved algorithm. Considering the retrieval performance across different vegetation types, future work will prioritize the semi-arid region, facilitating the creation of a long-term and spatially continuous C-band 1 km VOD dataset.

6. Conclusion

The objective of this study was to evaluate the performance of Sentinel-1 high-resolution VOD retrieval during 2016–2022 over ISMN. This was achieved by employing the WCM in conjunction with the semi-empirical Dubois model. Initially, a constant roughness parameter was calibrated by considering the period preceding vegetation growth. However, the evaluation is constrained by the given constant roughness estimates, which limit the VOD retrieval due to the limited variability of soil characterization. The Sentinel-1 VOD data were retrieved on an annual basis, and the retrieved results were then subjected to evaluation against vegetation indices (NDVI and EVI). These indices were considered as proxies of VOD. The evaluation results suggest that the algorithm is effective in capturing temporal changes of the observed vegetation dynamics, with average $R_{NDVI} = 0.77$ and $R_{EVI} = 0.78$. In particular, retrieved VOD demonstrates a higher correlation with VIs over grassland ($R_{NDVI} = 0.79$, $R_{EVI} = 0.79$) than other land types. These results showed the substantial capacity of retrieved VOD to facilitate the studies of global vegetation feature changes.

The results found over ISMN sites suggest that the proposed method could be extended to produce large-scale VOD by high-resolution (Xing et al. 2025) or downscaled soil moisture datasets (Lakshmi and Fang 2023). Furthermore, the development of a particular version of the algorithm could be accompanied by the improvement of soil backscatter models (Chen et al. 2003; Fung, Li, and Chen 1992): less uncertainty in the simulation of the soil backscatter and calibration of soil parameters could be obtained by a physics-based VOD model. In addition, the VOD retrieved from this algorithm depends on active backscatter observations. As such, it could be used to compare with passive VOD datasets. Moreover, other more appropriate Sentinel-1 preprocess workflow will be promoted in the future, which could be used to enhance the performance of VOD retrievals based on the process proposed in this study.

Author contributions

Lei Fan, Xiangzhuo Liu, Xiaojing Bai, Zanpin Xing, and Zhixuan Lu designed the experiment. Zhixuan Lu and Lei Fan conducted the analysis and wrote the manuscript. Jean-Pierre Wigneron, Frédéric Frappart, Nicolas Baghdadi, Jiangyuan Zeng, Jian Peng, Gabrielle De Lannoy, Xiaojun Li, Zhuangzhuang Feng and Xin Li revised the manuscript and provided valuable suggestions. All authors contributed to the discussion and revised the submitted manuscript. All authors agree to be accountable for all aspects of the work.

Disclosure statement

No potential conflict of interest was reported by the author(s).

Funding

This work was supported by research grants from the National Natural Science Foundation of China [grant numbers 42171339, 42322103], Fundamental Research Funds for the Central Universities [grant number SWU-KT25028], and the Chongqing Outstanding Youth Science Foundation [grant number CSTB2024NSCQ-JQX0010].

Data availability statement

The data that support the findings of this study are available from the corresponding authors, Lei Fan, upon reasonable request.

References

Attema, E., and F. T. Ulaby. 1978. "Vegetation Modeled as a Water Cloud." *Radio Science* 13 (2): 357–364. https://doi.org/10.1029/RS013i002p00357.

Atwood, D. K., H.-E. Andersen, B. Matthiss, and F. Holecz. 2014. "Impact of Topographic Correction on Estimation of Aboveground Boreal Biomass Using Multi-temporal, L-Band Backscatter." *IEEE Journal of Selected Topics in Applied Earth Observations and Remote Sensing* 7 (8): 3262–3273. https://doi.org/10.1109/JSTARS.2013.2289936.

Aubert, M., N. N. Baghdadi, M. Zribi, K. Ose, M. El Hajj, E. Vaudour, and E. Gonzalez-Sosa. 2012. "Toward an Operational Bare Soil Moisture Mapping Using TerraSAR-X Data Acquired over Agricultural Areas." *IEEE Journal of Selected Topics in Applied Earth Observations and Remote Sensing* 6 (2): 900–916. https://doi.org/10.1109/JSTARS.2012.2220124.

Bai, X., and B. He. 2015. "Potential of Dubois Model for Soil Moisture Retrieval in Prairie Areas Using SAR and Optical Data." *International Journal of Remote Sensing* 36 (22): 5737–5753. https://doi.org/10.1080/01431161.2015.1103920.

Bazzi, H., N. Baghdadi, P. Nino, R. Napoli, S. Najem, M. Zribi, and E. Vaudour. 2024. "Retrieving Soil Moisture from Sentinel-1: Limitations over Certain Crops and Sensitivity to the First Soil Thin Layer." *Water* 16 (1): 40. https://doi.org/10.3390/w16010040.

Benninga, H.-J. F., R. van der Velde, and Z. Su. 2019. "Impacts of Radiometric Uncertainty and Weather-Related Surface Conditions on Soil Moisture Retrievals with Sentinel-1." *Remote Sensing* 11 (17): 2025. https://doi.org/10.3390/rs11172025.

Boitard, S., A. Mialon, S. Mermoz, N. J. Rodríguez-Fernández, P. Richaume, J. C. Salazar-Neira, S. Tarot, and Y. H. Kerr. 2024. "Aboveground Biomass Dataset from SMOS L-Band Vegetation Optical Depth and Reference Maps." *Earth System Science Data* 17:1101–1119. https://doi.org/10.5194/essd-17-1101-2025.

Chang, Z., L. Fan, J.-P. Wigneron, Y.-P. Wang, P. Ciais, J. Chave, R. Fensholt, et al. 2023. "Estimating Aboveground Carbon Dynamic of China Using Optical and Microwave Remote-Sensing Datasets from 2013 to 2019." *Journal of Remote Sensing* 3. https://doi.org/10.34133/remotesensing.0005.

Chen, K.-S., T.-D. Wu, L. Tsang, Q. Li, J. Shi, and A. K. Fung. 2003. "Emission of Rough Surfaces Calculated by the Integral Equation Method with Comparison to Three-Dimensional Moment Method Simulations." *IEEE Transactions on Geoscience and Remote Sensing* 41 (1): 90–101. https://doi.org/10.1109/TGRS.2002.807587.

Didan, K. 2015a. "MOD13A2 MODIS/Terra Vegetation Indices 16-Day L3 Global 1 km SIN Grid V006." http://doi.rog/10.5067MODIS/mod13a2.006.

Didan, K. 2015b. "MYD13A2 MODIS/Aqua Vegetation Indices 16-Day L3 Global 1 km SIN Grid V006." http://doi.rog/10.5067MODIS/myd13a2.006.

Di Gregorio, A. 2005. *Land Cover Classification System: Classification Concepts and User Manual: LCCS*. Rome: Food & Agriculture Org.

Dobson, M. C., F. T. Ulaby, M. T. Hallikainen, and M. A. El-Rayes. 1985. "Microwave Dielectric Behavior of wet Soil-Part II: Dielectric Mixing Models." *IEEE Transactions on Geoscience and Remote Sensing* 1:35–46. https://doi.org/10.1109/TGRS.1985.289498.

Dorigo, W., I. Himmelbauer, D. Aberer, L. Schremmer, I. Petrakovic, L. Zappa, W. Preimesberger, A. Xaver, F. Annor, and J. Ardö. 2021. "The International Soil Moisture Network: Serving Earth System Science for over a Decade." *Hydrology and Earth System Sciences* 2021:1–83. https://doi.org/10.5194/hess-25-5749-2021.

Dorigo, W., W. Wagner, R. Hohensinn, S. Hahn, C. Paulik, A. Xaver, A. Gruber, M. Drusch, S. Mecklenburg, and P. Van Oevelen. 2011. "The International Soil Moisture Network: A Data Hosting Facility for Global in Situ Soil Moisture Measurements." *Hydrology and Earth System Sciences* 15 (5): 1675–1698. https://doi.org/10.5194/hess-15-1675-2011.

Dorigo, W., A. Xaver, M. Vreugdenhil, A. Gruber, A. Hegyiova, A. D. Sanchis-Dufau, D. Zamojski, C. Cordes, W. Wagner, and M. Drusch. 2013. "Global Automated Quality Control of in Situ Soil Moisture Data from the International Soil Moisture Network." *Vadose Zone Journal* 12 (3): 1–21. https://doi.org/10.2136/vzj2012.0097.

Dubois, P. C., J. Van Zyl, and T. Engman. 1995. "Measuring Soil Moisture with Imaging Radars." *IEEE Transactions on Geoscience and Remote Sensing* 33 (4): 915–926. https://doi.org/10.1109/36.406677.

El Hajj, M., N. Baghdadi, J. P. Wigneron, M. Zribi, C. Albergel, J. C. Calvet, and I. Fayad. 2019. "First Vegetation Optical Depth Mapping from Sentinel-1 C-Band SAR Data over Crop Fields." *Remote Sensing* 11 (23): 2769. https://doi.org/10.3390/rs11232769.

Fan, L., J. P. Wigneron, Q. Xiao, A. Al-Yaari, J. Wen, N. Martin-StPaul, J. L. Dupuy, et al. 2018. "Evaluation of Microwave Remote Sensing for Monitoring Live Fuel Moisture Content in the Mediterranean Region." *Remote Sensing of Environment* 205:210–223. https://doi.org/10.1016/j.rse.2017.11.020.

Fan, L., G. Dong, F. Frappart, J.-P. Wigneron, Y. Yue, X. Xiao, Y. Zhang, et al. 2024. "Satellite-Observed Increase in Aboveground Carbon over Southwest China during 2013-2021." *Journal of Remote Sensing* 4. https://doi.org/10.34133/remotesensing.0113.

Filipponi, F. 2019. "Sentinel-1 GRD Preprocessing Workflow." In *Proceedings*.
Frappart, F., J.-P. Wigneron, X. Li, X. Liu, A. Al-Yaari, L. Fan, M. Wang, et al. 2020. "Global Monitoring of the Vegetation Dynamics from the Vegetation Optical Depth (VOD): A Review." *Remote Sensing* 12 (18): 2915. https://doi.org/10.3390/rs12182915.
Fung, A. K., Z. Li, and K.-S. Chen. 1992. "Backscattering from a Randomly Rough Dielectric Surface." *IEEE Transactions on Geoscience and Remote Sensing* 30 (2): 356–369. https://doi.org/10.1109/36.134085.
Jones, M. O., L. A. Jones, J. S. Kimball, and K. C. McDonald. 2011. "Satellite Passive Microwave Remote Sensing for Monitoring Global Land Surface Phenology." *Remote Sensing of Environment* 115 (4): 1102–1114. https://doi.org/10.1016/j.rse.2010.12.015.
Lakshmi, V., and B. Fang. 2023. "SMAP-Derived 1-km downscaled surface soil moisture product, Version 1." NASA National Snow and Ice Data Center Distributed Active Archive Center (DAAC) data set, U8QZ2AXE5V7B. http://doi.rog/10.5067U8QZ2AXE5V7B.
Lane, J., and J. Saxton. 1952. "Dielectric Dispersion in Pure Polar Liquids at Very High Radio Frequencies - III. The Effect of Electrolytes in Solution." *Proceedings of the Royal Society of London. Series A. Mathematical and Physical Sciences* 214 (1119): 531–545. https://doi.org/10.1098/rspa.1952.0187.
Lawrence, H., J.-P. Wigneron, P. Richaume, N. Novello, J. Grant, A. Mialon, A. Al Bitar, O. Merlin, D. Guyon, and D. Leroux. 2014. "Comparison between SMOS Vegetation Optical Depth Products and MODIS Vegetation Indices over Crop Zones of the USA." *Remote Sensing of Environment* 140:396–406. https://doi.org/10.1016/j.rse.2013.07.021.
Li, X., J.-P. Wigneron, L. Fan, F. Frappart, S. H. Yueh, A. Colliander, A. Ebtehaj, et al. 2022. "A New SMAP Soil Moisture and Vegetation Optical Depth Product (SMAP-IB): Algorithm, Assessment and Inter-comparison." *Remote Sensing of Environment* 271: 112921. https://doi.org/10.1016/j.rse.2022.112921.
Li, X., J.-P. Wigneron, F. Frappart, L. Fan, P. Ciais, R. Fensholt, D. Entekhabi, et al. 2021. "Global-scale Assessment and Inter-comparison of Recently Developed/Reprocessed Microwave Satellite Vegetation Optical Depth Products." *Remote Sensing of Environment* 253:112208. https://doi.org/10.1016/j.rse.2020.112208.
Liu, C., and J. Shi. 2016. "Estimation of Vegetation Parameters of Water Cloud Model for Global Soil Moisture Retrieval Using Time-Series L-Band Aquarius Observations." *IEEE Journal of Selected Topics in Applied Earth Observations and Remote Sensing* 9 (12): 5621–5633. https://doi.org/10.1109/jstars.2016.2596541.
Liu, X., J.-P. Wigneron, W. Wagner, F. Frappart, L. Fan, M. Vreugdenhil, N. Baghdadi, et al. 2023. "A New Global C-Band Vegetation Optical Depth Product from ASCAT: Description, Evaluation, and Inter-comparison." *Remote Sensing of Environment* 299:113850. https://doi.org/10.1016/j.rse.2023.113850.
Liu, X. Z., J. P. Wigneron, L. Fan, F. Frappart, P. Ciais, N. Baghdadi, M. Zribi, et al. 2021. "ASCAT IB: A Radar-Based Vegetation Optical Depth Retrieved from the ASCAT Scatterometer Satellite." *Remote Sensing of Environment* 264:112587. https://doi.org/10.1016/j.rse.2021.112587.
Peng, C., J. Zeng, K.-S. Chen, H. Ma, H. Letu, X. Zhang, P. Shi, and H. Bi. 2024. "Spatial Representativeness of Soil Moisture Stations and Its Influential Factors at a Global Scale." *IEEE Transactions on Geoscience and Remote Sensing* 63: 1–15. https://doi.org/10.1109/TGRS.2024.3523484.
Poggio, L., L. M. De Sousa, N. H. Batjes, G. B. Heuvelink, B. Kempen, E. Ribeiro, and D. Rossiter. 2021. "SoilGrids 2.0: Producing Soil Information for the Globe with Quantified Spatial Uncertainty." *Soil* 7 (1): 217–240. https://doi.org/10.5194/soil-7-217-2021.
Qin, Y., X. Xiao, J.-P. Wigneron, P. Ciais, M. Brandt, L. Fan, X. Li, et al. 2021. "Carbon Loss from Forest Degradation Exceeds that from Deforestation in the Brazilian Amazon." *Nature Climate Change* 11 (5): 442. https://doi.org/10.1038/s41558-021-01026-5.
Rodríguez-Fernández, N. J., A. Mialon, S. Mermoz, A. Bouvet, P. Richaume, A. Al Bitar, A. Al-Yaari, M. Brandt, T. Kaminski, and T. Le Toan. 2018. "An Evaluation of SMOS L-Band Vegetation Optical Depth (L-VOD) Data Sets: High Sensitivity of L-VOD to Above-Ground Biomass in Africa." *Biogeosciences (Online)* 15 (14): 4627–4645. https://doi.org/10.5194/bg-15-4627-2018.
Rötzer, K., C. Montzka, D. Entekhabi, A. G. Konings, K. A. McColl, M. Piles, and H. Vereecken. 2017. "Relationship between Vegetation Microwave Optical Depth and Cross-Polarized Backscatter from Multiyear Aquarius Observations." *IEEE Journal of Selected Topics in Applied Earth Observations and Remote Sensing* 10 (10): 4493–4503. https://doi.org/10.1109/JSTARS.2017.2716638.
Schmidt, L., M. Forkel, R.-M. Zotta, S. Scherrer, W. A. Dorigo, A. Kuhn-Regnier, R. van der Schalie, and M. Yebra. 2023. "Assessing the Sensitivity of Multi-frequency Passive Microwave Vegetationoptical Depth to Vegetation Properties." *Biogeosciences (Online)* 20 (5): 1027–1046. https://doi.org/10.5194/bg-20-1027-2023.
Schmidt, T., M. Schrön, Z. Li, T. Francke, S. Zacharias, A. Hildebrandt, and J. Peng. 2024. "Comprehensive Quality Assessment of Satellite- and Model-Based Soil Moisture Products against the COSMOS Network in Germany." *Remote Sensing of Environment* 301:113930. https://doi.org/10.1016/j.rse.2023.113930.
Tian, F., M. Brandt, Y. Y. Liu, A. Verger, T. Tagesson, A. A. Diouf, K. Rasmussen, C. Mbow, Y. Wang, and R. Fensholt. 2016. "Remote Sensing of Vegetation Dynamics in Drylands: Evaluating Vegetation Optical Depth (VOD) Using AVHRR NDVI and in Situ Green Biomass Data over West African Sahel." *Remote Sensing of Environment* 177:265–276. https://doi.org/10.1016/j.rse.2016.02.056.
Todd, S., R. Hoffer, and D. Milchunas. 1998. "Biomass Estimation on Grazed and Ungrazed Rangelands Using Spectral Indices." *International Journal of Remote Sensing* 19 (3): 427–438. https://doi.org/10.1080/014311698216071.

Torres, R., P. Snoeij, D. Geudtner, D. Bibby, M. Davidson, E. Attema, P. Potin, et al. 2012. "GMES Sentinel-1 Mission." *Remote Sensing of Environment* 120:9–24. https://doi.org/10.1016/j.rse.2011.05.028.

van der Velde, R., Z. Su, P. van Oevelen, J. Wen, Y. Ma, and M. S. Salama. 2012. "Soil Moisture Mapping over the Central Part of the Tibetan Plateau Using a Series of ASAR WS Images." *Remote Sensing of Environment* 120:175–187. https://doi.org/10.1016/j.rse.2011.05.029.

Vreugdenhil, M., W. A. Dorigo, W. Wagner, R. A. De Jeu, S. Hahn, and M. J. Van Marle. 2016. "Analyzing the Vegetation Parameterization in the TU-Wien ASCAT Soil Moisture Retrieval." *IEEE Transactions on Geoscience and Remote Sensing* 54 (6): 3513–3531. https://doi.org/10.1109/TGRS.2016.2519842.

Vreugdenhil, M., C. Navacchi, B. Bauer-Marschallinger, S. Hahn, S. Steele-Dunne, I. Pfeil, W. Dorigo, and W. Wagner. 2020. "Sentinel-1 Cross Ratio and Vegetation Optical Depth: A Comparison over Europe." *Remote Sensing* 12 (20): 3404. https://doi.org/10.3390/rs12203404.

Wang, H., L. Yu, L. Chen, Z. Zhang, X. Li, N. Liang, C. Peng, and J.-S. He. 2023. "Carbon Fluxes and Soil Carbon Dynamics Along a Gradient of Biogeomorphic Succession in Alpine Wetlands of Tibetan Plateau." *Fundamental Research* 3 (2): 151–159. https://doi.org/10.1016/j.fmre.2022.09.024.

Wang, J., S. Zhang, Y. Zhao, F. Cai, C. Wang, J. He, and L. Ding. 2024. "Coseismic Deformation Analysis of the 2017 Milin Ms 6.9 Earthquake in the Namche Barwa Syntaxis: Implications for Regional Tectonics." *Fundamental Research* 24: TC3001. https://doi.org/10.1016/j.fmre.2024.09.003.

Wigneron, J.-P., P. Ciais, X. Li, M. Brandt, J. G. Canadell, F. Tian, H. Wang, A. Bastos, L. Fan, and G. Gatica. 2024. "Global Carbon Balance of the Forest: Satellite-Based L-VOD Results over the Last Decade." *Frontiers in Remote Sensing* 5:1338618. https://doi.org/10.3389/frsen.2024.1338618.

Xing, Z., L. Fan, L. Zhao, G. De Lannoy, F. Frappart, J. Peng, X. Li, et al. 2021. "A First Assessment of Satellite and Reanalysis Estimates of Surface and Root-Zone Soil Moisture over the Permafrost Region of Qinghai-Tibet Plateau." *Remote Sensing of Environment* 265:112666. https://doi.org/10.1016/j.rse.2021.112666.

Xing, Z., L. Zhao, L. Fan, G. De Lannoy, X. Bai, X. Liu, J. Peng, F. Frappart, K. Yang, and X. Li. 2025. "Retrieval of 1km Surface Soil Moisture from Sentinel-1 over Bare Soil and Grassland on the Qinghai-Tibetan Plateau." *Remote Sensing of Environment* 318:114563. https://doi.org/10.1016/j.rse.2024.114563.

Yang, H., P. Ciais, F. Frappart, X. Li, M. Brandt, R. Fensholt, L. Fan, S. Saatchi, S. Besnard, and Z. Deng. 2023. "Global Increase in Biomass Carbon Stock Dominated by Growth of Northern Young Forests over Past Decade." *Nature Geoscience* 16 (10): 886–892. https://doi.org/10.1038/s41561-023-01274-4.

Zanaga, D., R. Van De Kerchove, D. Daems, W. De Keersmaecker, C. Brockmann, G. Kirches, J. Wevers, O. Cartus, M. Santoro, and S. Fritz. 2022. "ESA WorldCover 10 m 2021 v200." http://doi.rog/10.5281zenodo.7254221.

Zhang, C., S. Gao, W. Li, K. Bi, N. Huang, Z. Niu, and G. Sun. 2020. "Radiometric Calibration for Incidence Angle, Range and sub-footprint Effects on Hyperspectral LiDAR Backscatter Intensity." *Remote Sensing* 12 (17): 2855. https://doi.org/10.3390/rs12172855.

Zhong, S., L. Fan, G. De Lannoy, F. Frappart, J. Zeng, M. Vreugdenhil, J. Peng, et al. 2024. "Quantitative Assessment of Various Proxies for Downscaling Coarse-Resolution VOD Products over the Contiguous United States." *International Journal of Applied Earth Observation and Geoinformation* 130:103910. https://doi.org/10.1016/j.jag.2024.103910.

Zhou, Z., L. Fan, G. De Lannoy, X. Liu, J. Peng, X. Bai, F. Frappart, et al. 2022. "Retrieval of High-Resolution Vegetation Optical Depth from Sentinel-1 Data over a Grassland Region in the Heihe River Basin." *Remote Sensing* 14 (21): 5468. https://doi.org/10.3390/rs14215468.

Zhu, L., J. P. Walker, N. Ye, and C. Rüdiger. 2019. "Roughness and Vegetation Change Detection: A Pre-Processing for Soil Moisture Retrieval from Multi-temporal SAR Imagery." *Remote Sensing of Environment* 225:93–106. https://doi.org/10.1016/j.rse.2019.02.027.

Zribi, M., N. Baghdadi, N. Holah, and O. Fafin. 2005. "New Methodology for Soil Surface Moisture Estimation and Its Application to ENVISAT-ASAR Multi-incidence Data Inversion." *Remote Sensing of Environment* 96 (3-4): 485–496. https://doi.org/10.1016/j.rse.2005.04.005.